ADVANCED FUNCTIONAL MATERIALS
www.afm-journal.de

3D Printed Fractal Metamaterials with Tunable Mechanical Properties and Shape Reconfiguration

Dong Wang, Le Dong, and Guoying Gu**

Lattice metamaterials constructed by curved microstructures exhibit large stretchability and are promising in soft electronics and soft robotics. Fractal structures are particularly efficient in improving stretchability as it shows multiple-order uncurling. However, the development of fractal metamaterials is hindered by hierarchical structures and large deformations. In this study, a design framework combining experiments, hierarchical theoretical models, and finite element simulations is developed to program the mechanical behaviors of fractal metamaterials. For 3D printing, a digital design tool is developed to visualize the structure and automatically generate the manufacturing representations. Results show that large stretchability (≈360%), bionic stress–strain curve matching, and imperfection insensitivity can be programmed by tuning the geometric parameters. An integrated device of an electromyogram sensor embedded in an imperfection-insensitive fractal metamaterial that matches the J-shaped stress–strain curve of human skin is demonstrated. Light-emitting diode devices based on fractal metamaterial with shape reconfiguration are also presented. This st paves a new way to realize multifunctional soft devices using fractal metamaterials.

1. Introduction

Lattice metamaterials, consisting of periodic arranged building blocks, exhibit exceptional properties and functionalities that differ from and surpass those of their constituent materials.[1–6] Inspired by the wavy filaments in stretchable biological materials, lattice metamaterials constructed by curved microstructures are designed to exhibit large stretchability, which shows promising applications in soft electronics and soft robotics.[7–10] For example, horseshoe lattices with mechanics precisely match the conventional J-shaped stress–strain curves of human skin are developed.[11,12] To expand the design space, lattice metamaterials constructed by parametric curves have been proposed.[13–15] When subjected to external loadings, the curves bend, rotate, and uncurl, increasing the stretchability.

Compared to the one-order uncurling of the basic curves, the fractal-inspired designs are particularly efficient in improving stretchability as they show multiple-order uncurling.[16–18] Fractals are self-similar structures at all levels and are ubiquitous in nature and engineering.[19–22] Typical examples include the fractal transporting networks of trees and the fractal airway branches in the lungs,[23,24] lightweight load-bearing architecture,[25–27] antenna array [28,29] and superhydrophobic nanostructures.[30,31] Fractal metamaterials can be formed by replacing the straight beams in crisscross lattice with fractal microstructures, which may significantly improve stretchability.

However, the development of fractal metamaterials is hindered due to the lack of theoretical models and digital design tools. Theoretical models that interrelate the three hierarchical structures are needed to program the mechanical properties such as Young's modulus and Poisson's ratios. But it is complicated by the intricate geometry and the large deformation. Additive manufacturing enables the precise fabrication of complex lattices that would not be possible otherwise.[32–35] The manufacturing representation (typically as STL file) is usually needed and generated by computer-aided design (CAD) tools. While most commercial CAD tools are able to design simple lattices, fast and efficient digital design tools for complex fractal structures are still lacking.

Furthermore, current lattice structures generally lack shape reconfigurability. Once manufactured, the mechanical properties and geometry of the metamaterials are fixed without the ability to adapt and adjust, which significantly limits the application of the lattice structures. By printing the 3D structures with active materials, the structures can change their configurations subjected to an external stimulus.[35–37] The incorporation of the shape reconfiguration further intricates the design of fractal metamaterials. Therefore, the digital design and hierarchical modeling for fractal structures with programmable mechanical properties and shape reconfigurability are needed.

In this work, we develop a digital design tool and theoretical modeling method to program the mechanical behaviors of fractal metamaterials. The complete workflow from CAD,

D. Wang, L. Dong, G. Gu
Robotics Institute, School of Mechanical Engineering
Shanghai Jiao Tong University
Shanghai 200240, China
E-mail: wang_dong@sjtu.edu.cn; guguoying@sjtu.edu.cn

D. Wang, L. Dong, G. Gu
State Key Laboratory of Mechanical System and Vibration
Shanghai Jiao Tong University
Shanghai 200240, China

D. Wang, L. Dong, G. Gu
Meta Robotics Institute
Shanghai Jiao Tong University
Shanghai 200240, China

The ORCID identification number(s) for the author(s) of this article can be found under https://doi.org/10.1002/adfm.202208849.

DOI: 10.1002/adfm.202208849

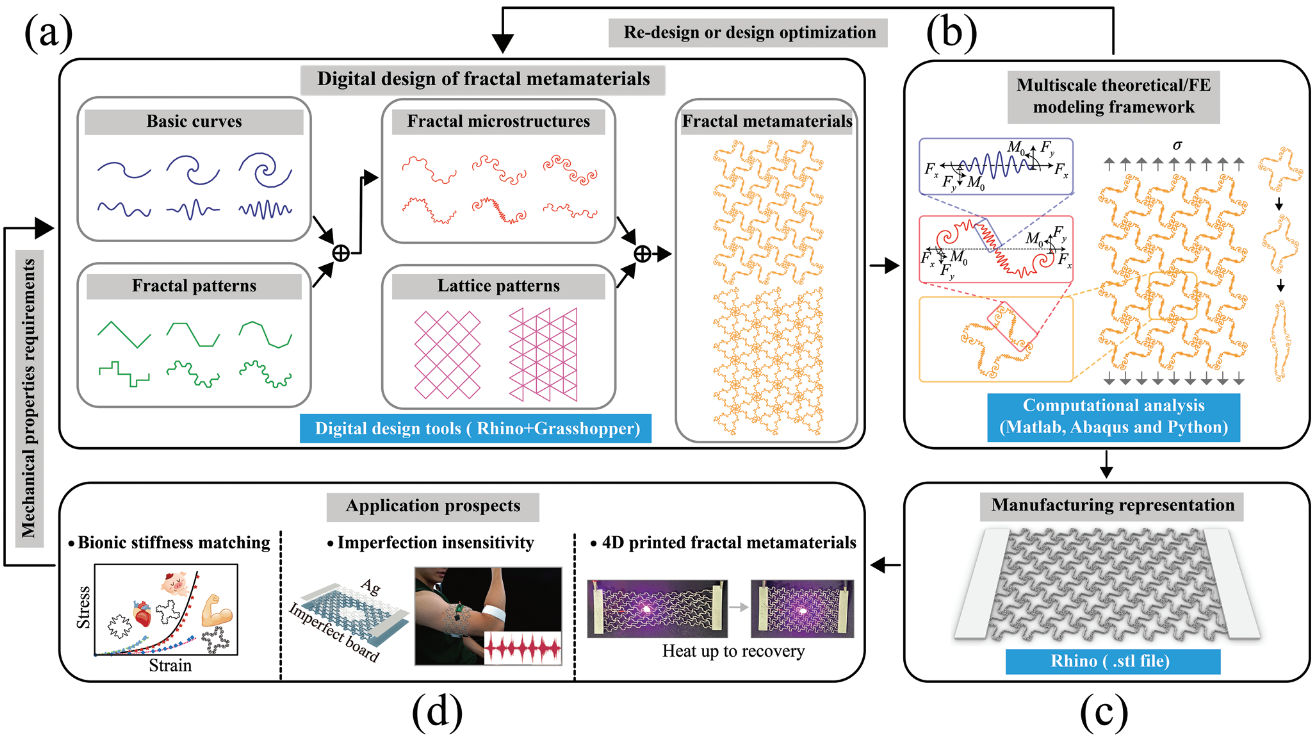

Figure 1. The design framework for fractal metamaterials. The main workflow includes a) digital design of fractal metamaterials, b) hierarchical theoretical/FE modeling framework, c) generation of the manufacturing representation, and d) 3D printed fractal metamaterials with demonstrated application prospects.

to theoretical modeling, to 3D printing and applications on stretchable electronics is enabled. First, the fractal metamaterials are designed by replacing the straight beams in a crisscross lattice using the fractal microstructures, which are formed by interconnecting the basic curves following a fractal pattern (**Figure 1**a). Second, a combined experimental, theoretical and finite element (FE) design framework is developed to program their mechanical behaviors. Three theoretical models are developed for the basic curves, fractal microstructure, and fractal metamaterials successively, which take into account the hierarchical structure and large deformation (Figure 1b). Third, we develop a digital design tool to visualize the structures and automatically generate the STL files. The STL files are then output to a PolyJet 3D printer for high-resolution manufacturing using a shape memory polymer (Figure 1c,d), enabling the realization of multifunctionalities and shape reconfigurability.

The combined experimental, theoretical, and FE method enable the programmable mechanical properties of the fractal metamaterials. Results show that large stretchability (≈360%, >17 times the same lattice built from straight beams) and bionic stress–strain curve matching can be programmed by tuning the geometric parameters. Moreover, the fractal metamaterials increase the imperfection insensitivity significantly, overcoming the failure difficulty faced in real situations where hole imperfections are generally necessary to accommodate hard, inorganic electronic components. We demonstrate an integrated device of an electromyogram sensor embedded in an imperfect fractal metamaterial that matches the J-shaped stress–strain curve of human skin. We also demonstrate Light-emitting diode (LED) devices based on fractal metamaterials with shape reconfigurations. This work paves a new way to realize multifunctional soft devices using fractal metamaterials.

2. Digital Design of the Fractal Metamaterials

Figure 1a depicts the structural design of the fractal metamaterials. Fractal metamaterials with rectangular and triangular lattice patterns are presented. The fractal metamaterials consist of three hierarchical structures: the basic curves, the fractal microstructures, and the fractal metamaterials. First, the antisymmetric basic curves are designed using parametric functions, enabling the generations of various curled microstructures in Cartesian coordinate. Second, the fractal microstructure is formed by interconnecting the same or different types of basic curves in a fractal pattern. Lastly, the fractal metamaterial is formed by replacing the straight beams with fractal microstructures in a crisscross lattice.

We develop a computer-aided design tool for visualization and manufacturing. The design tool is implemented in the 3D modeling software Rhinoceros using the algorithmic design environment Grasshopper (Movie S1, Supporting Information). It consists of the following four steps: 1) the formation of basic curves using parametric functions, 2) the generation of fractal microstructures using basic curves, 3) generating fractal metamaterials by replacing the straight beams in a lattice with fractal microstructures, and 4) the generation of STL representations for 3D printing. A screenshot of the CAD environment and the designed structures is presented in Figure S1 (Supporting Information). In this way, the complex fractal structures can be visualized based on the input geometric parameters, and the STL files can be automatically generated for 3D printing.

3. Hierarchical Theoretical Model of Fractal Metamaterials

Being able to design the structures of fractal metamaterials with geometric parameters, we want to model their mechanical properties and enable a model-based design approach for such structures before their actual physical realization through 3D printing. A hierarchical theoretical framework is developed, which includes three theoretical models for the basic curves, fractal microstructures and fractal metamaterials, respectively. Here we derive the three models successively. Details are given in the Supporting Information.

3.1. Modeling of Basic Curves

Consider a basic curve designed by the parametric function $X = \Psi(t)$ and $Y = \varsigma(t)$, where $t_0 \le t \le t_{end}$. The basic curve is simply supported and deformed under horizontal force F_x, vertical force F_y and moment M_0 at each end (**Figure 2**a). Using the force and moment balance, the governing equation of the basic curve can be written as (Section 2.1 in Supporting Information)

$$\theta'' = (\theta' - \alpha')\frac{R'}{R} + R^2\alpha'^2 f(\theta) + \frac{\theta'\alpha''}{\alpha'} \tag{1}$$

where θ and α are the deformed and undeformed slope angles. The prime denotes the differentiation with respect to t. R and α are

$$R = R(t) = \frac{[\psi'^2(t) + \zeta'^2(t)]^{\frac{3}{2}}}{[\psi'(t)\zeta''(t) - \psi''(t)\zeta'(t)]} \text{ and } \alpha = \alpha(t) = \arctan\frac{\zeta'(t)}{\psi'(t)} \tag{2}$$

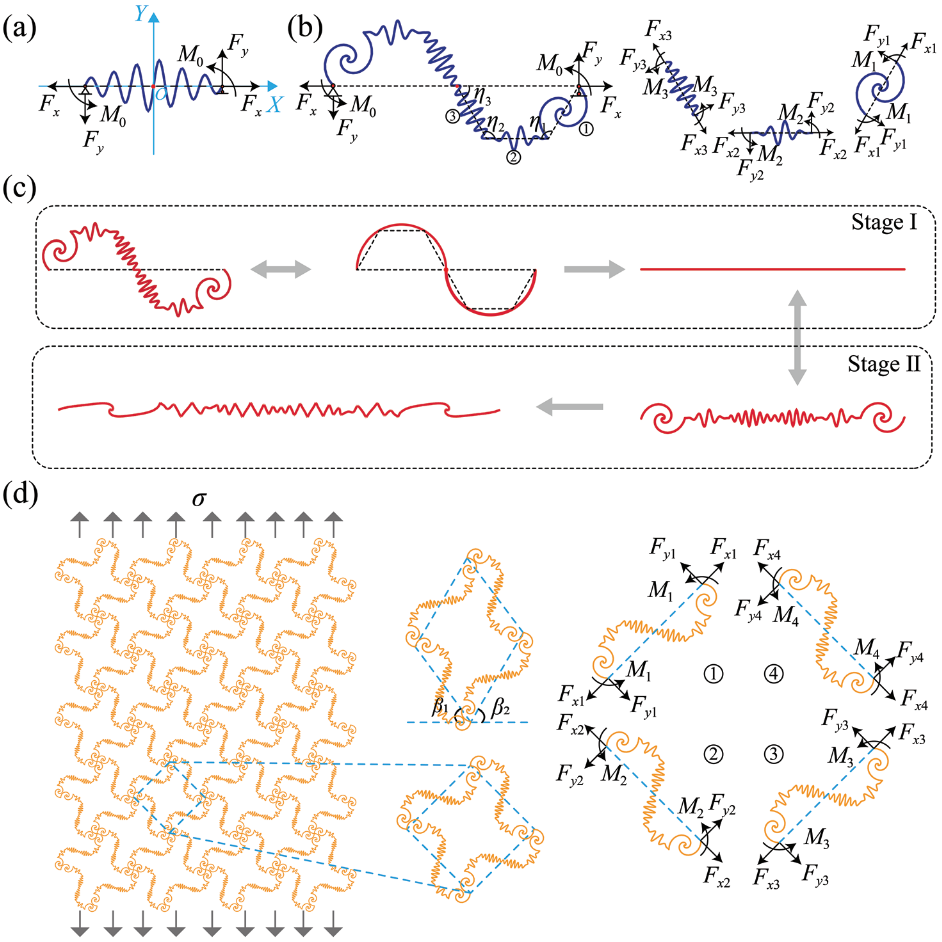

Figure 2. Schematic illustration of the hierarchical theoretical model for the fractal metamaterial. a) A simply supported basic curve subject to a horizontal force F_x, vertical force F_y and a pair of antisymmetric moments M_0. b) An antisymmetric fractal microstructure composed of six basic curves under applied forces and moments. c) Two stages of the orderly unraveling of the fractal microstructure. d) Schematics of a rectangular fractal metamaterial under uniaxial vertical stress σ. The undeformed and deformed shapes of a representative unit are shown. Inner forces and moments for each microstructure are also presented.

Equation (1) is a second-order ordinary differential equation of θ and can be solved using two boundary conditions. The deformed coordinates x and y of the basic curve can then be obtained as

$$\begin{pmatrix} x \\ y \end{pmatrix} = \int_{t_0}^{t} (1+\varepsilon) R\alpha' \begin{pmatrix} \cos\theta \\ \sin\theta \end{pmatrix} dt \tag{3}$$

where ε is the axial strain.

3.2. Modeling of Fractal Microstructures

We take a fractal microstructure composed of six basic curves as an example. The structure is depicted in Figure 2b. η_1 and η_2 are the angles between the two adjacent microstructures, and η_3 is the angle between microstructure 3 and the horizontal axis. γ_i and L_i (i = 1, 2, and 3) are the corresponding angles and horizontal lengths of the microstructure after deformation, respectively.

Previous research [11] has proven that the deformation of fractal microstructures follows a mechanism of ordered unraveling and can be divided into two stages (Figure 2c). In stage I, fractal patterns are first expanded by in-plane bending, while the basic curves hardly deform. In stage II, the fractal pattern has been fully expanded, and the deformation behavior is transformed into the unraveling of the basic curves.

In stage I, the fractal microstructure is modeled as the equivalent fractal pattern. Equation (1) gives the governing equation of fractal pattern's deformation behavior during stage I. The critical strain at stage I can be provided by

$$\varepsilon_I = \frac{\sum_1^3 \widehat{L}_i - L_0}{L_0} \tag{4}$$

where L_0 is the half of the initial horizontal length of the fractal microstructures. $\widehat{L}_i$ is the distance between the two ends of the basic curves. In stage II, we focus on unraveling of the basic curves. The static equilibrium requires that the inner force at the joint between each microstructure in both X and Y directions yields (Figure 2b)

$$\begin{pmatrix} 1 & 0 & 0 & 0 & 0 & 0 \\ 0 & 1 & 0 & 0 & 0 & 0 \\ -\cos(\pi-\gamma_1) & \sin(\pi-\gamma_1) & 1 & 0 & 0 & 0 \\ -\sin(\pi-\gamma_1) & -\cos(\pi-\gamma_1) & 0 & 1 & 0 & 0 \\ 0 & 0 & -\cos(\pi-\gamma_2) & \sin(\pi-\gamma_2) & 1 & 0 \\ 0 & 0 & -\sin(\pi-\gamma_2) & -\cos(\pi-\gamma_2) & 0 & 1 \end{pmatrix} \begin{pmatrix} F_{x1} \\ F_{y1} \\ F_{x2} \\ F_{y2} \\ F_{x3} \\ F_{y3} \end{pmatrix} = \begin{pmatrix} F_x \cos(2\pi - \sum_1^3 \gamma_i) + F_y \sin(2\pi - \sum_1^3 \gamma_i) \\ F_y \cos(2\pi - \sum_1^3 \gamma_i) - F_x \sin(2\pi - \sum_1^3 \gamma_i) \\ 0 \\ 0 \\ 0 \\ 0 \end{pmatrix}. \tag{5}$$

During deformation, the angles between the tangent directions of corresponding connected microstructures remain unchanged. Thus, it gives

$$\begin{pmatrix} 1 & 0 \\ 0 & 1 \end{pmatrix} \begin{pmatrix} \gamma_1 \\ \gamma_2 \end{pmatrix} + \begin{pmatrix} 1 & -1 & 0 \\ 0 & 1 & -1 \end{pmatrix} \begin{pmatrix} \theta_1 \\ \theta_2 \\ \theta_3 \end{pmatrix} = \begin{pmatrix} \eta_1 \\ \eta_2 \end{pmatrix} \tag{6}$$

To maintain geometric compatibility, the following geometric relations should be satisfied

$$L_y = L_3 \sin\gamma_3 + L_2 \sin\left(\sum_2^3 \gamma_i - \pi\right) + L_1 \sin\left(\sum_1^3 \gamma_i - 2\pi\right) = 0 \tag{7}$$

By solving Equations (5)–(7) and the governing equations of the basic curves (Equation (1)), the 15 unknowns F_{xi}, F_{yi}, γ_i, θ_i, L_i (i = 1, 2, and 3) can be solved. Note that the mechanical behaviors of fractal microstructures with general configurations are derived in Supporting Information.

3.3. Modeling of Fractal Metamaterials

The theoretical model for fractal metamaterials under longitudinal vertical load σ_y is studied. A rectangular fractal metamaterial is taken as an example. As shown in Figure 2d, the representative unit of the fractal metamaterial is composed of four microstructures (indexed from 1 to 4), where the angles β_i (i = 1–4) characterize the rigid-body motion of each microstructure. $\widehat{L}$ is the distance between the two ends of the microstructures. Due to the anti-symmetry of the rectangular unit, fractal microstructures 1 and 3 or 2 and 4 have the same deformation behaviors. The static equilibrium of the representative unit gives the relationships among the inner forces and the external loading in both X and Y directions:

$$\begin{pmatrix} \cos\beta_2 & -\sin\beta_2 & \cos\beta_1 & \sin\beta_1 \\ -\sin\beta_2 & -\cos\beta_2 & \sin\beta_1 & -\cos\beta_1 \\ -\cos\beta_2 & \sin\beta_2 & \cos\beta_1 & \sin\beta_1 \\ \sin\beta_2 & \cos\beta_2 & \sin\beta_1 & -\cos\beta_1 \end{pmatrix} \begin{pmatrix} F_{x1} \\ F_{y1} \\ F_{x2} \\ F_{y2} \end{pmatrix} = \begin{pmatrix} 0 \\ 0 \\ 0 \\ \sqrt{2}\sigma_y \widehat{L} d \end{pmatrix} \tag{8}$$

The moment equilibrium of an arbitrary joint connected by four microstructures requires that

$$\sum_{i=1}^{4} M_i = -\sum_{i=1}^{4} (F_{yi} L_i)/2 = 0 \tag{9}$$

The angle between the tangent directions of two connected fractal microstructures remains unchanged during deformation. Thus we have:

$$\beta_1 + \beta_2 + \theta_1 - \theta_2 = \pi/2 \tag{10}$$

The deformed configurations of fractal metamaterials can be obtained by solving Equations (8)–(10) and the governing equations of the fractal microstructures Equations (1) and (5)–(7). The longitudinal strain ε_y and Poisson's ratio ν can be written as

$$\varepsilon_y = \frac{L_1 \sin\beta_2 + L_2 \sin\beta_1 - \sqrt{2}\widehat{L}}{\sqrt{2}\widehat{L}} \tag{11}$$

$$\nu = \frac{L_1 \cos\beta_2 + L_2 \cos\beta_1 - \sqrt{2}\widehat{L}}{L_1 \sin\beta_2 + L_2 \sin\beta_1 - \sqrt{2}\widehat{L}} \tag{12}$$

4. Validation of the Model

4.1. Validation for the Fractal Microstructures

Experiments and FE simulations are conducted to validate the theory model for the fractal microstructures first. The experimental, theoretical and FE simulated results of a basic curve and three fractal microstructures subjected to uniaxial tensile loadings are shown in **Figure 3**a-d. The geometric parameters are w = 0.2 mm, $\widehat{L}/w = 150\sqrt{2}$ and d/w = 6. The basic curve is designed by $R(\alpha) = \alpha^2 (0 \le \alpha \le 4.1)$ (Figure 3a). The fractal microstructure I consists of six identical basic curves (Figure 3b). In Figure 3c, the fractal microstructure II is composed of eight basic curves with two different types. Six basic curves with three different types are interconnected to form the fractal microstructure III (Figure 3d). The detailed designed functions and geometric parameters can be found in Figure S4 (Supporting Information).

The microstructures exhibit nonlinear J-shaped stress–strain curves. The deformations of the microstructures are bending-dominated and show a low effective modulus at the "toe region", while they are stretching-dominated with a large modulus at the "linear region". Fractal microstructures are generally more stretchable than basic curves due to the orderly unraveling. For example, the stretchability of the fractal microstructures I, II, and III are ≈100%, ≈88%, and ≈230%, which is significantly larger than the basic curves (≈40%). The mechanical behaviors of the fractal microstructures depend significantly on the fractal pattern and the configuration of the basic curves. Different fractal microstructures also exhibit remarkable differences resulting from the various combinations of basic curves. The theoretical predictions agree reasonably well with the experimental and FEM simulated results (Movie S2, Supporting Information).

The deformed shapes of the fractal microstructures II and III are shown in Figure 3e,f. The comparison between the experimental, theoretical and FE simulated shapes of the basic curves and fractal microstructure I can be found in Figure S5 (Supporting Information). The ordered unraveling of the fractal microstructure can be observed. At stage I (the axial strain $\varepsilon <$ 30% for type II and the axial strain $\varepsilon <$ 50% for type III), the deformation of the microstructure is mainly due to the expansion of the fractal pattern. As the strain further increases, the deformation is dominated by unraveling the basic curves.

4.2. Validation for the Fractal Metamaterials

Experiments are then conducted to validate the theoretical model for the fractal metamaterials. Figure 3g compares the theoretical (red dots), experimental (blue stars) and FE simulated (black curves) results of rectangular fractal metamaterials subjected to uniaxial tensile loadings. The fractal metamaterial is built by the fractal microstructure III shown in Figure 3a. 4 × 3 periodical units are used in the rectangular fractal metamaterials.

Similar to the fractal microstructures, the fractal metamaterials also display nonlinear J-shaped stress–strain curves. The experimental and FE simulated deformed shapes at strains of 75% and 150% are shown in Figure 3h. The theoretically predicted deformed shapes of the representative units are also compared. We can observe that all the experimental, theoretical and FE simulated stress–strain curves and deformed shapes agree well. We also observe that the rectangular metamaterial exhibits a positive Poisson's ratio, while the triangular metamaterial shows a negative Poisson's ratio (Figure S7 and Movie S3, Supporting Information).

The stretchability of the fractal metamaterials depends significantly on the fractal microstructures. A highly stretchable fractal metamaterial is designed and tested as shown in Figure S6 (Supporting Information). Its failure strain is ≈360%, >17 times the same lattice built from straight beams.

5. Application Prospects

The validated theoretical/FE framework can be further used to guide the design of fractal metamaterials. The tunable stiffness and Poisson's ratio, bionic stress–strain curves matching, imperfection insensitivity, and shape reconfigurability of the fractal metamaterials are studied. Application prospects on soft electronics are demonstrated.

5.1. Tunable Stiffness and Poisson's Ratio

The stiffness and Poisson's ratio can be tuned by varying the geometric parameters. Metamaterials constructed using both the basic curves and fractal microstructures are designed. The basic curves are designed using a parametric function $Y(X) = X^a(X\text{–}b)$. By varying the parameters a and b, the shapes of the basic curves change continuously. The shape of corresponding rectangular and triangular metamaterials with different a and b are shown in **Figure 4**a. The change of the arc length on a and b is shown in Figure 4b.

The dependence of the stiffness and Poisson's ratio on a and b are studied. Figure 4c,d (top row) show the contour plot of the axial strain of the rectangular metamaterials under σ = 300 kPa. The increase of the axial strain (indicating lower stiffness) follows similar trends to the increase of the arc length. For example, the rectangular metamaterials with b = 2.5 are softer than those with b = 0.5, due to the dense curling of the microstructures. Triangular metamaterials also follow a similar trend (Figure 4e,f, top row).

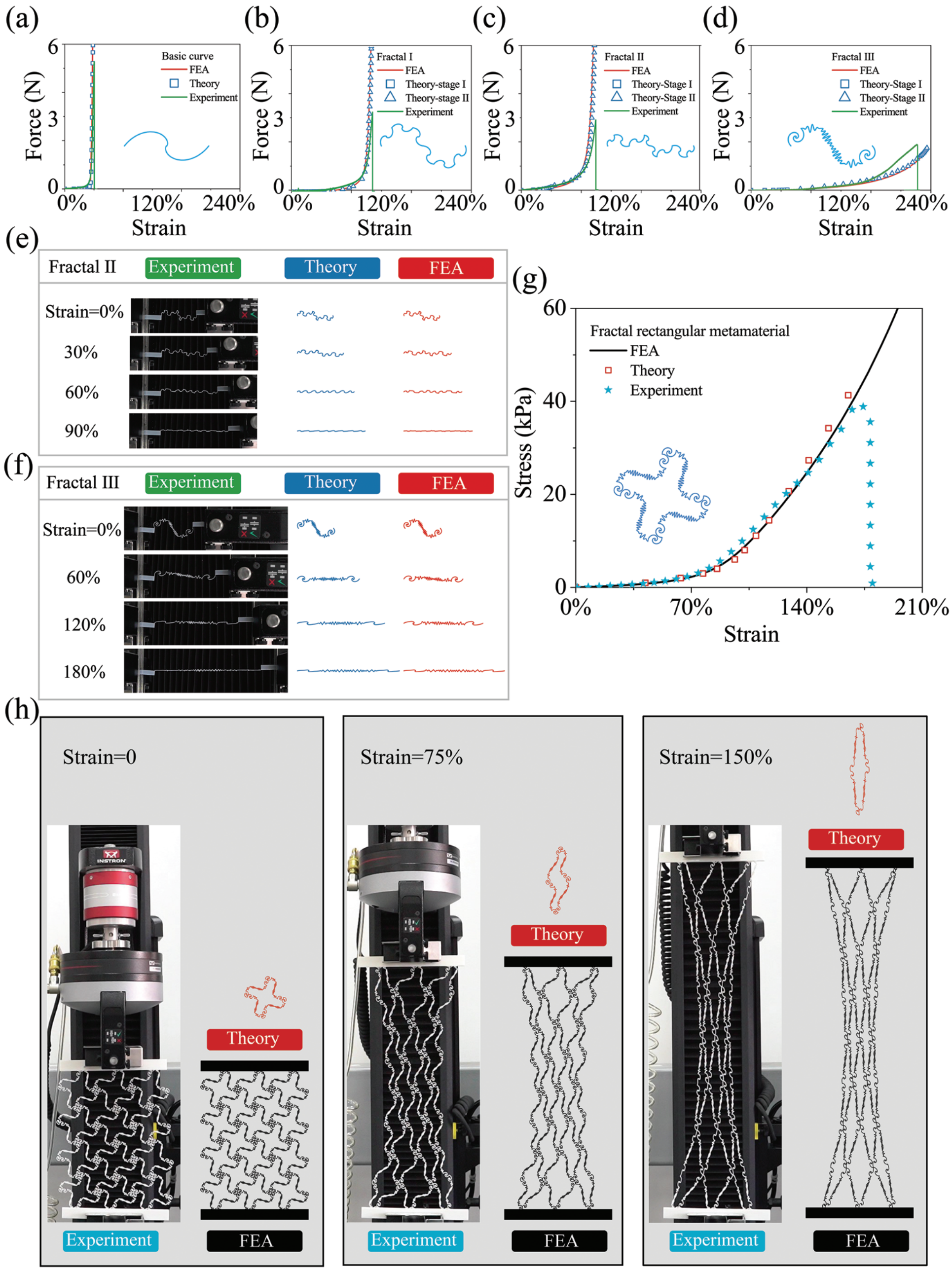

Figure 3. Validation of the hierarchical theoretical models for the fractal metamaterials. The theoretical predicted, experimental and FE simulated stress–strain curves of a) a basic curve and b–d) three fractal microstructures are compared. e,f) The comparison between the experimental, theoretical and FE simulated deformed shapes of the fractal microstructures in (c) and (d). g) Comparison of fractal metamaterials' experimental, theoretical and FE simulated stress–strain curves. h) The experimental and FE simulated deformed shapes at 0, 75%, and 150% strains. The theoretical shapes of a representative unit are also shown.

The contour plots of the Poisson's ratio on a and b are also shown (the bottom row in Figure 4c–f). The rectangular metamaterials always exhibit positive Poisson's ratios. On the contrary, the triangular metamaterials show negative Poisson's ratios. By tuning a and b, the value of the Poisson's ratio varies. Fractal metamaterials designed by another function $Y(X) = (X - a)(X - 1)\sin(6\pi X/b)$, ($2 \le a \le 4, 2 \le b \le 4$) are shown in Figure S8 (Supporting Information). Results show that the Poisson's ratio of the triangular metamaterials can also be positive by varying the microstructures.

5.2. Bionic Stress–Strain Curves Matching and Inverse Optimization

The development of stretchable devices with mechanical responses matching the stress–strain curves of biological tissues is particularly important for long-term biointegration, as the discomfort induced by the mechanical mismatch is minimized. Biological tissues and organs generally exhibit large stretchability and strain-stiffening effect (J-shaped stress–strain

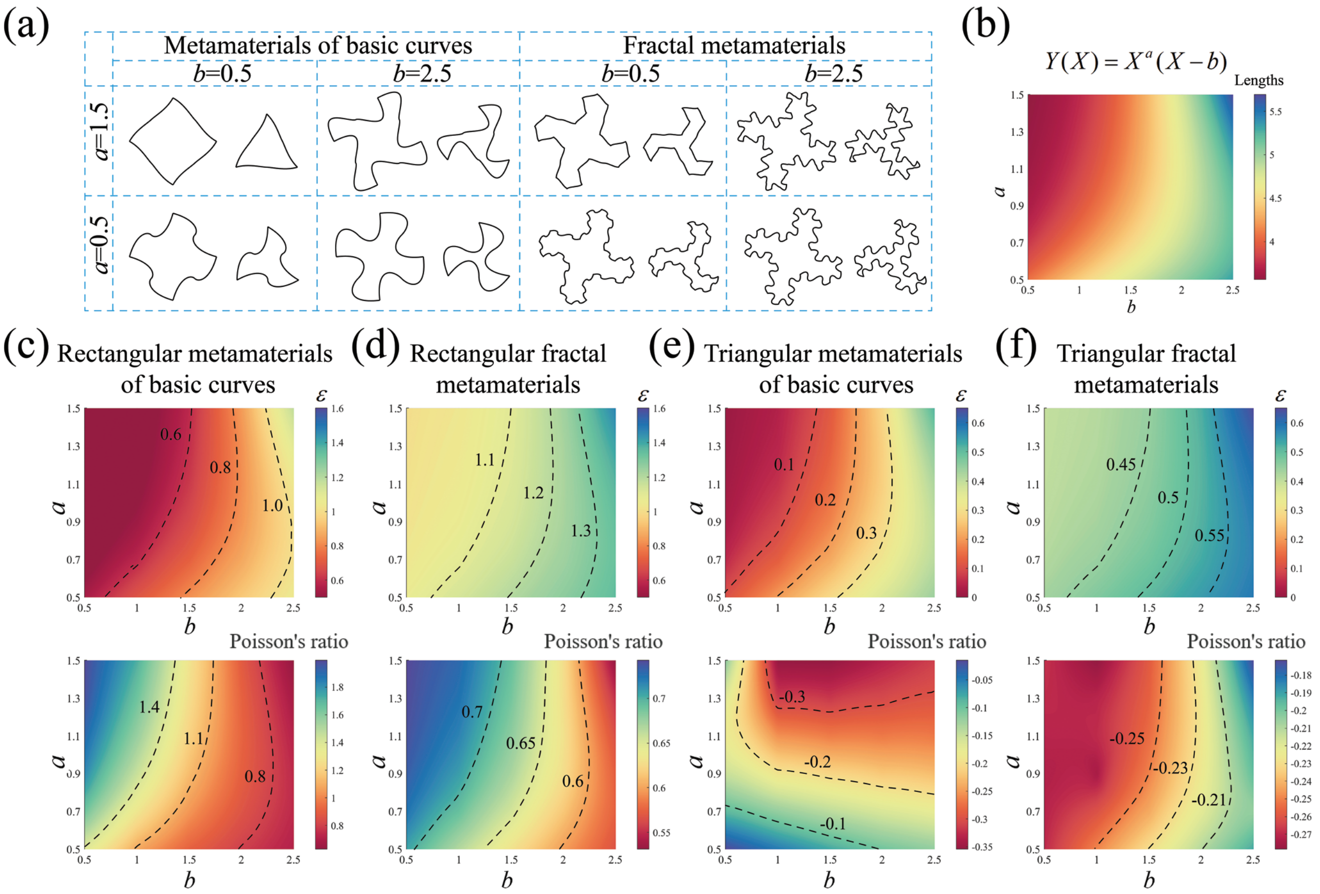

Figure 4. Tunable stiffness and Poisson's ratio of the metamaterials. a) The rectangular and triangular metamaterials constructed by the basic curves or fractal microstructures with different a and b. The basic curves are designed using $Y(X) = X^a(X - b)$ $(0.5 \le a \le 1.5,\ 0.5 \le b \le 2.5)$. b) The dependence of the arc lengths on a and b. c) and d) show the contour plot of the strain and the Poisson's ratio of rectangular metamaterials under $\sigma = 300$kPa. e) and f) show the contour plot of the strain and Poisson's ratio of triangular metamaterials under $\sigma = 180$kPa.

curves) to prevent damage from exposure to large deformations. The highly stretchable fractal metamaterials are potential candidates.

The theoretical and FE simulated stress–strain curves of four rectangular and four triangular metamaterials are shown in **Figure 5**a,b, respectively. It can be seen that a wide design space of stress–strain curves is formed by tuning both the microstructures and the fractal patterns. For example, the stiffness of the iliac artery, pig belly skin and muscle fiber can be reproduced by rectangular fractal metamaterials (Figure 5c). Triangular fractal metamaterials are able to replicate the nonlinear mechanical responses of the lens capsule, internal mammary artery and cat's skin in Figure 5d (data from ref. [38–40]). The stress–strain curves of these biological tissues can be accurately replicated. The structures of the optimal design and the detailed procedures are shown in the Supporting Information.

An optimization method is developed to obtain the desired stress–strain curve. As the relationship between the geometric parameters and the output stress–strain curves is highly nonlinear, machine learning (ML) and evolutionary algorithms (EA) can be combined to obtain the objective stress–strain curves fast and efficiently. The ML algorithm is used as a surrogated model, while the EA is adopted for fast inverse optimization. The procedures of the ML-EA optimization method are shown below.

First, a database is formed for the ML algorithm. The inputs are the geometric parameters, and the outputs are the corresponding stress–strain curves. We use four parameters a, b, f, and l, to generate different fractal metamaterials (**Figure 6**a). a and b are geometric parameters in the parametric functions of the basic microstructures $Y = X^a(X\text{-}b)$, where $a \in [0.5\ 1.5]$ and $b \in [0.5\ 2.5]$. f is the pattern type for fractal microstructure. Four patterns are used for f. l represents the type of lattice pattern, including rectangular ($l = 1$) and triangular ($l = 2$) lattice patterns. Note that a and b vary continuously within the set domain, and f and l are discrete values. The stress–strain curve of the generated fractal metamaterial is automatically computed using FE simulation. A database can then be built by varying the geometric parameters.

Next, the ML algorithm performs as a surrogate model to significantly decrease the computational cost. An ANN-based ML model is established by learning the databases, which maps the nonlinear relationship between the design parameters (a, b, f, and l) and stress–strain curves (Figure 6b). The network architecture consists of a feature input layer, three fully connected layers, and a regression layer. The adaptive moment estimation

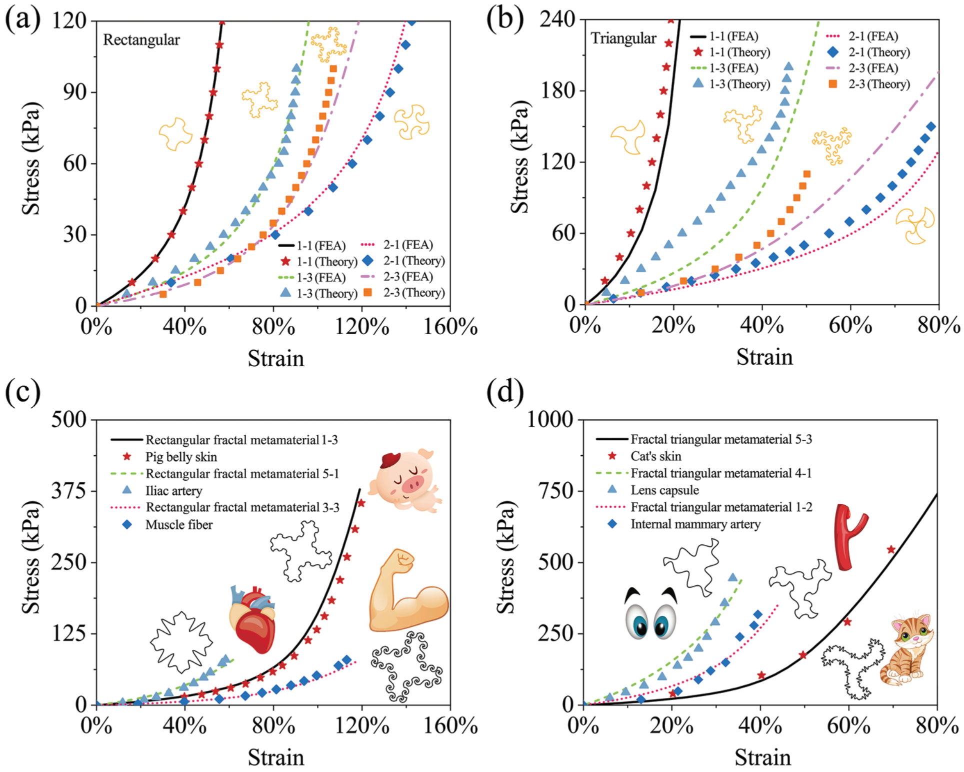

Figure 5. Bionic stress–strain curves matching: a) and b) show the comparison of theoretical and FEM simulated results of different fractal metamaterials. c) and d) present the J-shaped stress–strain curves of various tissues and organs accurately reproduced by the fractal metamaterials.

(Adam) optimizer and Rectified Linear Unit (ReLU) are applied in the ANN training process. The Mean Squared Error (MSE) performs as the loss function to evaluate the accuracy. The results show that the loss function converges to a steady state. The predicted and actual values conform to a high coefficient of determination ($R^2 = 0.9998$), indicating the high prediction accuracy of the established ML model.

Last, the EA algorithm is combined with the ML model to obtain optimal designs that satisfy the target stress–strain curve. EA is a biomimetic optimization algorithm inspired by natural selection that simulates the behavior of biological populations. Figure 6c shows the schematic illustration of the ML-EA optimization. The algorithm begins with the establishment of an initial generation with 200 individuals. Each individual represents a different fractal metamaterial. The individuals are evaluated by a fitness function, and the generation is then updated by selection, crossover, and mutation. The fitness function for a target stress–strain curve is set as:

$$F_1 = \sqrt{\frac{1}{m}\sum_{i=1}^{m}\left(y_1(x_i) - \hat{y}_1(x_i)\right)^2} \tag{13}$$

where m is the number of process goals to be satisfied. x_i are vectors that contains design parameters a, b, f, and l (constant to be optimized), and applied strain (variation). $y_1(x_i)$ are the target stress values and $\hat{y}_1(x_i)$ are the predicted stress values obtained by the ML model.

The bionic stress–strain curve of pig belly skin is used as the target stress–strain curve. Using the developed ML-EA method, the stress–strain curve can be reproduced by the optimal fractal metamaterial (Figure 6a). The optimized design parameters $a = 0.524$, $b = 2.478$, $f = 2$, and $l = 1$.

5.3. Imperfection Insensitivity of Fractal Metamaterials

When the lattice metamaterials are utilized as the substrate of bio-integrated electronics, holes are needed to accommodate hard, inorganic electronic components. Moreover, the microstructures may crack due to the continuously large and repeat deformations interacting with human skins. Both will introduce defects to the lattice metamaterials. In this subsection, the imperfection insensitivity of the fractal metamaterials is investigated.

Figure 7a–c compares the mechanical responses of the rectangular metamaterials with and without defects subjected to uniaxial tension. Rectangular metamaterials constructed by basic curves and fractal microstructure I are shown. Four typical imperfect configurations are presented: a small central hole (Imperfect I), a large central hole (Imperfect II), a large side crack (Imperfect III), and random defect distributions with a defect density 7.5% (Imperfect IV).

Figure 7b shows the J-shaped stress–strain curves of the perfect and imperfect metamaterials (Movie S4, Supporting Information). Here, we study the deviations of stress–strain curves

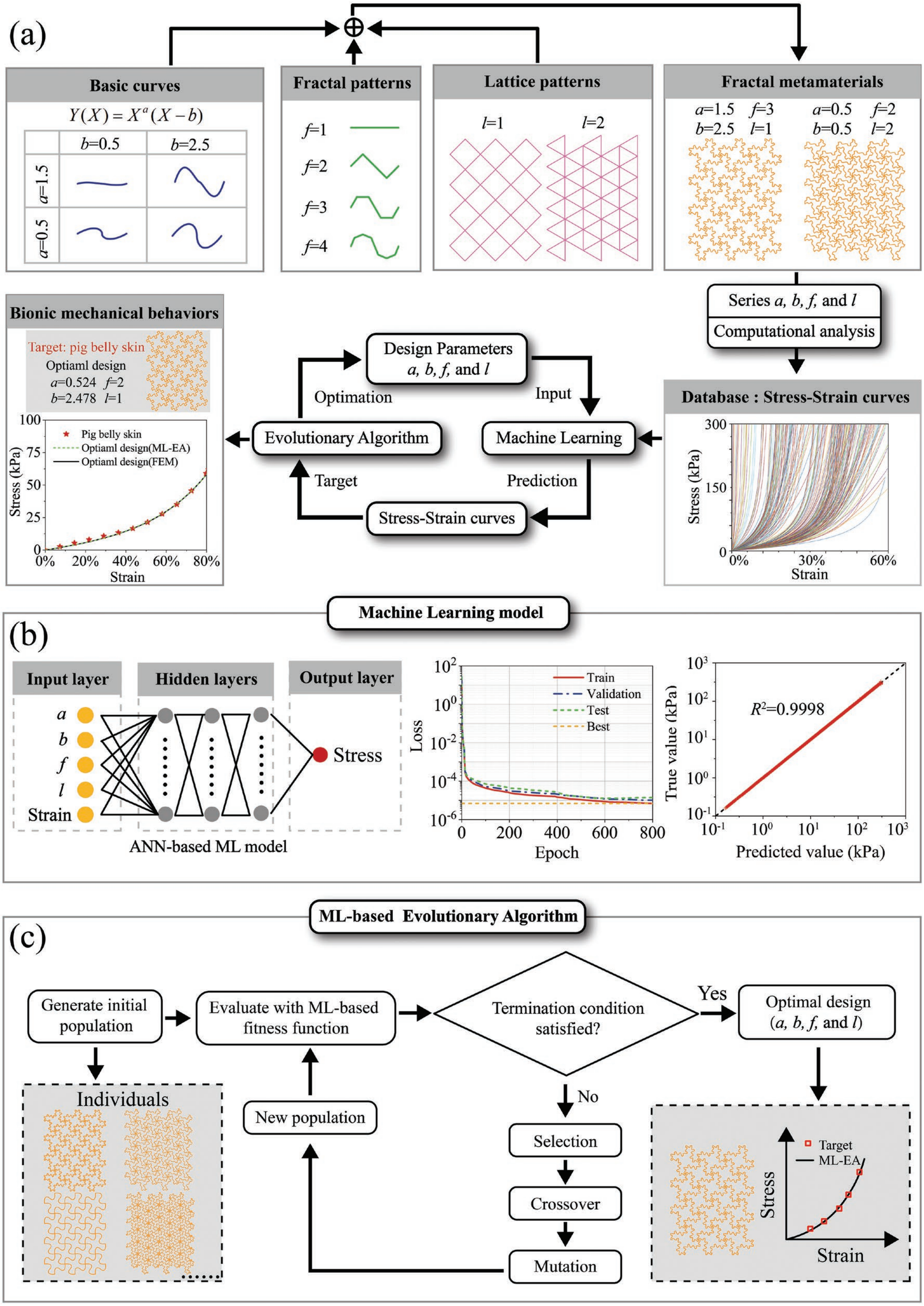

Figure 6. Inverse optimization of the bionic stress–strain curves. a) Four parameters a, b, f and l are used for the geometric patterns. A database is formed using python-assisted FEM. The ML method is then used as a surrogated model, and the GA is used for inverse optimization to find the target stress–strain curve. b) The architecture and performance of ANN-based ML model. The ANN model comprises the input layer, the hidden layers, and the output layer. The loss function converges to a steady state during the training process. The predicted and actual values conform to a high coefficient of determination ($R^2 = 0.9998$). c) Schematic illustration of the ML-EA optimization approach.

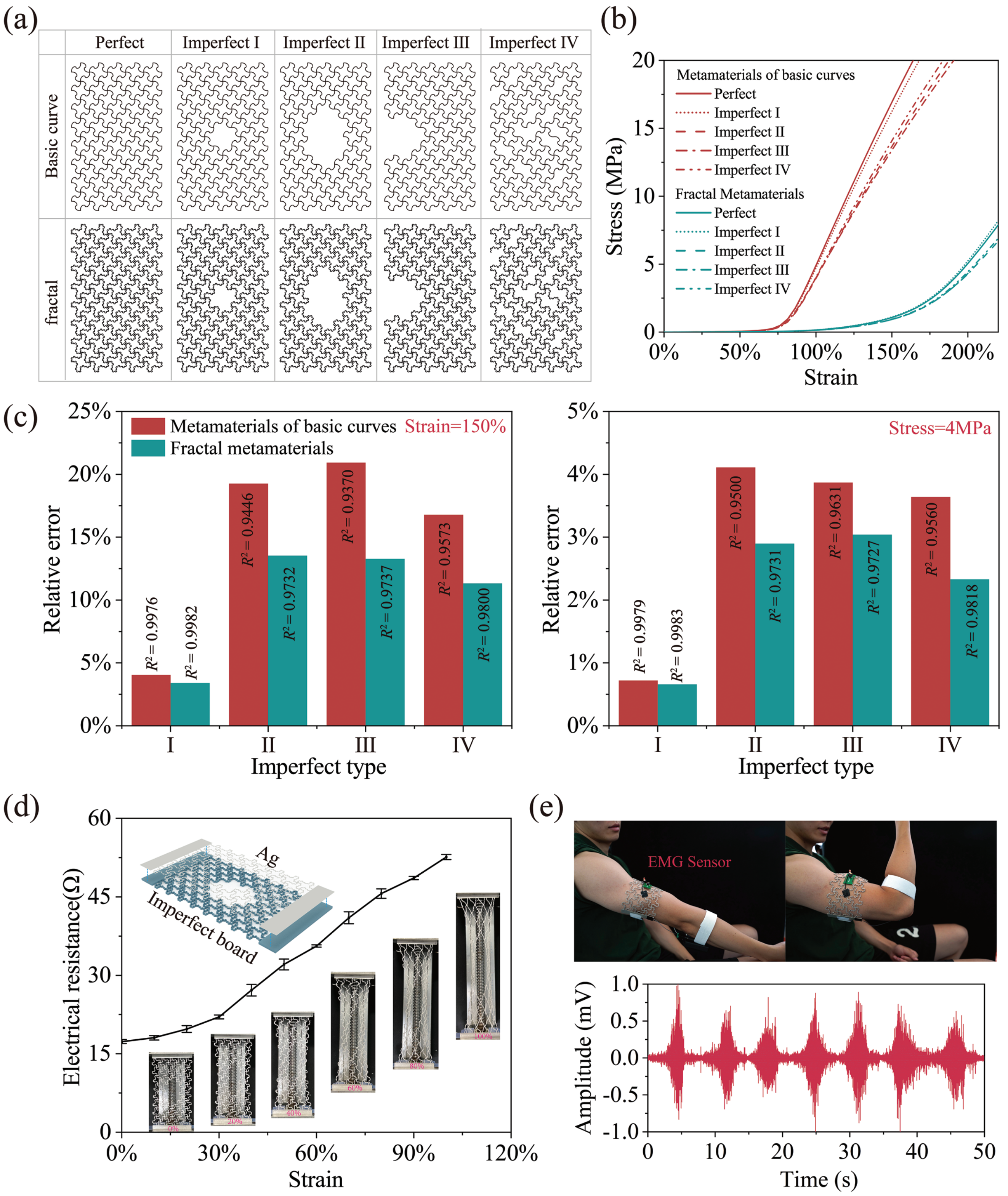

Figure 7. Imperfect-insensitive fractal metamaterials for stretchable flexible electronics. a) Schematics of perfect and imperfect fractal metamaterials. b) Comparison of FEM simulated stress–strain curves of different imperfect and perfect metamaterials under uniaxial stretching. c) shows the relative error and the coefficient of determination R^2 of the stress–strain curves between the imperfect and perfect metamaterials under a fixed strain or stress. d) The dependences of the resistance on the axial strains of the conductive imperfect metamaterials coated with a thin layer of silver. e) An integrated device of bionic electromyogram (EMG) sensors embedded in an imperfect fractal metamaterial that matches the J-shaped stress–strain behavior of human skin and collects bioelectrical signals of exercising human biceps.

due to the effect of imperfection in the strain domain (0%, 150%) and stress domain (0, 4 MPa), respectively. The coefficient of determination R^2 is used to evaluate the effect of the defect

$$R^2 = \frac{\sum_{i=1}^{n} (\hat{y}_i - \overline{y})^2}{\sum_{i=1}^{n} (y_i - \overline{y})^2} \tag{14}$$

where y_i represents the stress or strain of the perfect metamaterials; $\overline{y}$ is its average value and $\hat{y}_i$ is the corresponding value of the imperfect metamaterials. The closer R^2 to 1, the metamaterials are more insensitive to defects.

Figure 7c compares the relative errors (strain or stress) between the imperfect and perfect metamaterials under stress = 4 MPa or strain = 150%. The R^2 is also shown. The fractal metamaterials exhibit lower relative errors and a higher R^2 than the metamaterials constructed by only basic curves, indicating the fractal metamaterials are more insensitive to the defects. The R^2 of all the four types of imperfect fractal metamaterials is >0.97.

Figure 7d shows a conductive imperfect fractal metamaterial coated with a thin layer of silver. The resistance of the fractal metamaterial under tension is measured by a precision LCR meter (Keysight E4980AAL). The resistance increases by around three times when the axial strain is 100%. The optical images of the stretchable conductive metamaterial under tension are presented. It is worth noting that the metamaterial has a lightweight characteristic, which can be supported by a thin leaf (Figure S20, Supporting Information).

The combined property of imperfection insensitivity, bionic stiffness matching, conductive, and lightweight demonstrates their promise in stretchable electronics. Figure 7e shows an integrated device of a bionic electromyogram (EMG) sensor embedded in an imperfect fractal metamaterial. The designed fractal metamaterial with an initial central defect can accurately reproduce the J-shaped stress–strain behavior of human skin (Figure S12, Supporting Information). The EMG sensor is immobilized into the fractal metamaterials via cured Polydimethylsiloxane (PDMS). The result shows the integrated device can smoothly wrap the human arm and serve as a wearable sensor to collect bioelectrical signals of the human biceps (Movie S5, Supporting Information). Moreover, the fractal metamaterial can serve as a conductive substrate by coating a silver layer. A LED light is powered through the fractal metamaterial by a portable power supply. The imperfect fractal metamaterial matches the macroscopic topography of the skin surfaces during the experiment. The device demonstrated herein can also be used for human motion capture or health monitoring.

5.4. Conductive Fractal Metamaterials with Shape Reconfigurability

Most lattice metamaterials lack the ability to adapt and adjust. By printing the lattice metamaterials with active materials, they can change their configurations subjected to an external stimulus. The designed fractal metamaterials are printed using the material Vero. The dynamic mechanical analysis (DMA) of printed samples shows Vero is a shape memory polymer with a glassy transition temperature $T_g = \approx 60°C$ (**Figure 8**a), enabling shape reconfigurability design.

FE simulations are conducted to study the shape reconfigurability of two typical fractal metamaterials. The FE simulated shape memory cycles are shown in Figure 8b,c. The metamaterials are first stretched at a temperature (80 °C) higher than T_g. The temperature then decreases to 20 °C, and the external loading is removed. The deformed shapes are fixed in this step, called the programmed shapes. The metamaterials can restore their original shapes by applying external heating (Figure S17 and Movie S6, Supporting Information).

The structures of the fractal metamaterials provide diverse programmed shapes and multifunctionalities. Figure 8b shows the diverse programmed shapes of fractal structures in shape reconfiguration. Five programmed states are shown: compression, tension, bend, fold and torsion. In Figure 8b(ii), an in-plane compression is demonstrated. In Figure 8b(iii), the fractal metamaterials exhibit a highly stretched state. In Figure 8b(iv), the bend fractal metamaterials can carry a load of ≈200 g, 12 times its original weight. Complex 3D states such as fold and torsion are also programmed. Examples of programmed fractal metamaterials matching the stress–strain curves of different biological materials at different temperatures and showing programmable Poisson's ratios are shown in Figures S18 and S19 in Supporting Information.

LED devices based on rectangular and triangular fractal metamaterials with shape reconfigurability are presented (Figure 8e). LED lights are connected to the fractal metamaterials. An external DC power (5 V) is used to power the devices. The rectangular and triangular metamaterials are programmed with ε = 75% and ε = 40%, respectively. The lights are on, showing both fractal metamaterials are still conductive, as the local strain remains small although the overall strain is large. When a thermal stimulus is applied, the metamaterials recover to their initial shapes, and remains conductive. FE simulated shapes are also presented for comparison. The shape reconfigurability of the fractal metamaterials provides potential applications in reconfigurable flexible electronics.

6. Discussion and Conclusion

Inspired by nature, fractal structures with straight microstructures have been extensively used in engineering applications on different scales. Nevertheless, they generally lack stretchability and tunable stress–strain curves. Fractal structures with curved microstructures exhibit large stretchability and have already been used in flexible electronics.[17,41,42] However, the microstructures in the fractal structures generally follow simple geometric patterns, such as structures consisting of lines (Peano, Hilbert) and curves with constant curvatures (Moore, Greek cross). The use of simple structures limits mechanical properties such as large stretchability, tunable stiffness and negative Poisson's ratios.[43] Also, the fractal structures generally consist of a single curve. Hence, any imperfection in the fractal curves will lead to fatal damage, which is common due to the large and repeated deformation when interacting with biological tissues. Moreover, current fractal structures lack shape reconfigurability.

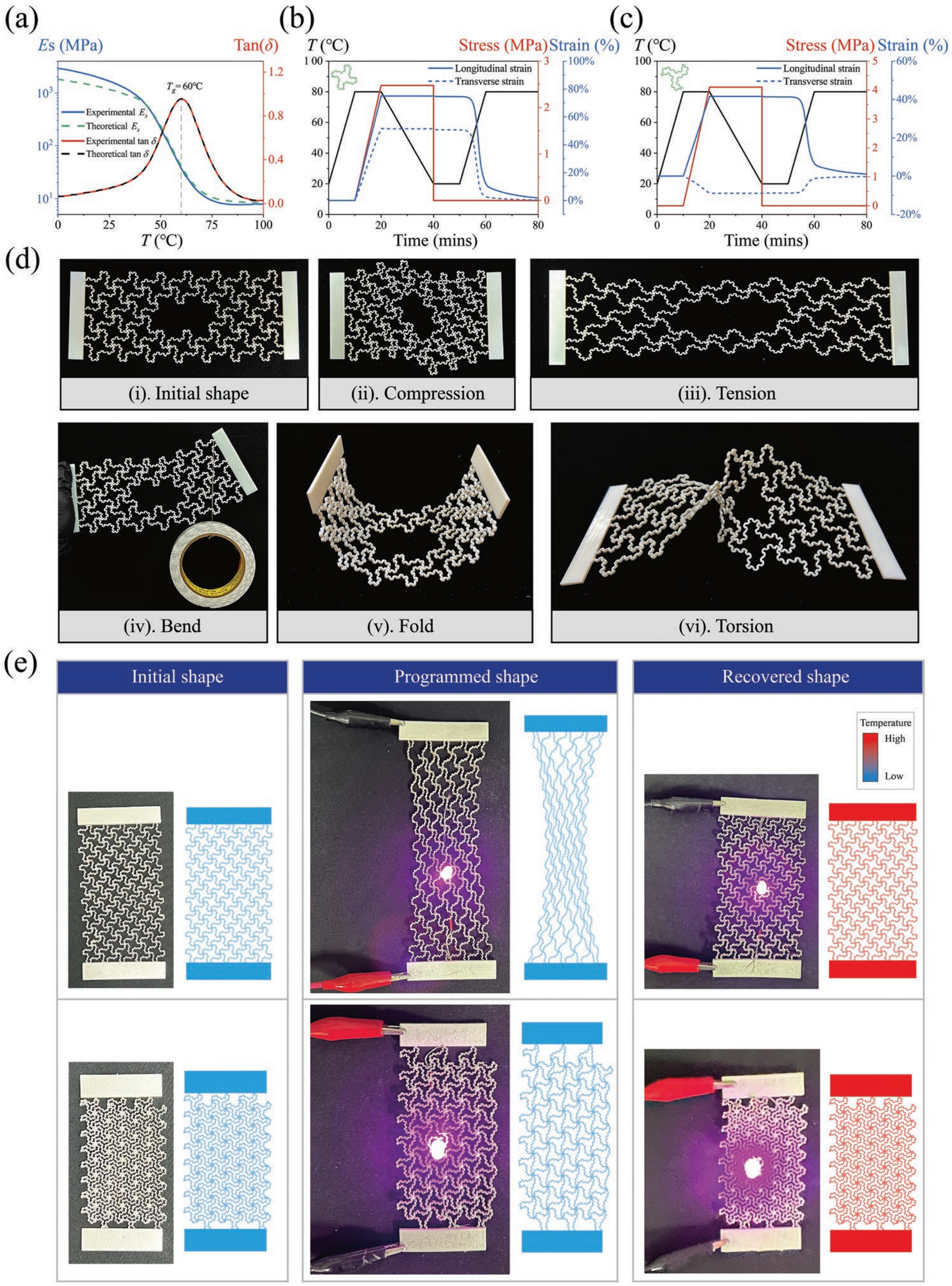

Figure 8. Shape reconfigurability of the fractal metamaterials. a) DMA test results of Vero and the corresponding theoretical fitting results using thermomechanical multi-branch model. b) and c) present the FEM simulated shape memory cycles of rectangular and triangular fractal metamaterials, respectively. d) Five programmed states are shown: compression, tension, bend, fold and torsion. e) shows LED devices based on rectangular and triangular fractal metamaterials with shape reconfigurability. The fractal metamaterials are conductive in different states. FEM results are shown for comparison.

Compared to these fractal structures, the design fractal metamaterials in this work exhibit programmable mechanical properties, imperfection-insensitivity and shape reconfigurability.

In summary, we develop a design framework combining experiments, a hierarchical theoretical model and finite element simulations to program the mechanical behaviors of the fractal metamaterials. We also develop a digital design tool to visualize the structure and automatically generate the STL files from geometric parameters for 3D printing. Fractal metamaterials that exhibit bionic stress–strain matching, imperfection insensitivity, conductivity and lightweight properties simultaneously can be integrated designed and manufactured. Main results include: 1) the fractal metamaterials exhibit an exceptional tensile performance of more than 360%, which is about 17 times that of lattices built from straight beams; 2) the J-shaped stress–strain curves of various biological tissues and organs can be matched due to the wide design space of the fractal metamaterials; 3) the fractal metamaterials exhibit excellent imperfection insensitivity under tension, with R^2 >0.97 for all the four types of imperfect fractal metamaterial; 4) by virtue of the shape memory effect of the Vero materials, the fractal metamaterials exhibit reconfigurable shape and adapt to the external environment under thermal stimulus. Using the integrated design and manufacturing framework, a device of a bionic electromyogram (EMG) sensor embedded in an imperfect fractal metamaterial is presented that matches the J-shaped stress–strain behavior of human skin and collects bioelectrical signals of exercising human biceps. LED devices with shape reconfigurability are also shown. This work paves a new way to realize multifunctional soft devices using fractal metamaterials.

7. Experimental Section

Fabrication: The fractal structures were fabricated using a commercial polyjet 3D printer (Object J750, Stratasys). Veroblue was chosen as the material with Young's modulus $E = 1.5$ GPa and Poisson's ratio $\nu = 0.3$ at room temperature. Veroblue is referred to as Vero for simplicity. The width of the microstructure was set to be larger or equal to 0.2 mm to ensure the designed lattice could be fabricated. Enough void (0.1 mm) between microstructures was kept to avoid self-intersection during printing. Dynamic mechanical analysis was conducted for the Vero material (Figure S15, Supporting Information). Results show that Vero is a shape memory polymer with glass transition temperature $T_g = \approx 60$ °C. 4D shape change can then be generated by applying thermal stimulus.

Finite Element Analysis: The commercial finite element software ABAQUS (3DS Dassault Systèmes, France) was employed to analyze the fractal metamaterial's mechanical behaviors and shape memory effects. The 3-node plane strain thermally coupled triangle element CPE3T was used. Quasi-static simulations were performed using Abaqus/Standard. The multi-branch model was used to capture the thermo-mechanical behaviors (details are shown in the Supporting Information). One end of the fractal metamaterial was fixed, and the displacement loading condition was applied to the other end.

Preparation of integrated bionic EMG Monitoring System: The EMG Monitoring System comprises a conductive imperfect fractal metamaterial (Figure S12, Supporting Information) and a dry-electrode surface EMG sensor (Sichiray, China) connected via PDMS. The PDMS was made by mixing the base material (Sylgard 184, Dow Corning) and the curing agent with a 15:1 weight ratio by the planetary centrifugal mixer (ARE-310, Thinky, USA) at 1500 rpm for 2 min. An LED light was attached to the end nodes of the defect of the fractal metamaterial. A portable 9 V lithium battery powered the device, and the sampling frequency iwas 1 kHz. The EMG signals were processed by Arduino UNO and sent to the host computer, which are read and displayed by MATLAB in real-time. The demonstration of bionic sensors has been given the informed written consent of the participant and approved by the Ethics Research Committee of the Shanghai Jiao Tong University.

Supporting Information

Supporting Information is available from the Wiley Online Library or from the author.

Acknowledgements

D.W. and L.D. contributed equally to this work. This work was supported by the National Natural Science Foundation of China (Grant Nos. 51905336, 52025057, 91848204), the Science and Technology Commission of Shanghai Municipality (Grant No. 20550712100), and the State Key Laboratory of Mechanical System and Vibration (grant no. MSVZD202212).

Conflict of Interest

The authors declare no conflict of interest.

Data Availability Statement

The data that support the findings of this study are available from the corresponding author upon reasonable request.

Keywords

fractal metamaterials, imperfection insensitivity, shape reconfiguration, tunable mechanical properties

Received: August 2, 2022
Revised: September 26, 2022

---

[1] H. Cui, D. Yao, R. Hensleigh, H. Lu, A. Calderon, Z. Xu, S. Davaria, Z. Wang, P. Mercier, P. Tarazaga, *Science* **2022**, *376*, 1287.
[2] M. Kadic, G. W. Milton, M. van Hecke, M. Wegener, *Nat. Rev. Phys.* **2019**, *1*, 198.
[3] M. C. Fernandes, J. Aizenberg, J. C. Weaver, K. Bertoldi, *Nat. Mater.* **2021**, *20*, 237.
[4] J. Cha, K. W. Kim, C. Daraio, *Nature* **2018**, *564*, 229.
[5] Y. Wang, L. Li, D. Hofmann, J. E. Andrade, C. Daraio, *Nature* **2021**, *596*, 238.
[6] S. Janbaz, N. Noordzij, D. S. Widyaratih, C. W. Hagen, L. E. Fratila-Apachitei, A. A. Zadpoor, *Sci. Adv.* **2017**, *3*, eaao1595.
[7] M. Pishvar, R. L. Harne, *Adv. Sci.* **2020**, *7*, 2001384.
[8] Y. Ling, W. Pang, J. Liu, M. Page, Y. Xu, G. Zhao, D. Stalla, J. Xie, Y. Zhang, Z. Yan, *Nat. Commun.* **2022**, *13*, 524.
[9] A. Rafsanjani, K. Bertoldi, A. R. Studart, *Sci. Rob.* **2019**, *4*, eaav7874.
[10] C. Yang, M. Boorugu, A. Dopp, J. Ren, R. Martin, D. Han, W. Choi, H. Lee, *Mater. Horiz.* **2019**, *6*, 1244.
[11] K.-I. Jang, H. U. Chung, S. Xu, C. H. Lee, H. Luan, J. Jeong, H. Cheng, G.-T. Kim, S. Y. Han, J. W. Lee, *Nat. Commun.* **2015**, *6*, 6566.
[12] Q. Ma, H. Cheng, K.-I. Jang, H. Luan, K.-C. Hwang, J. A. Rogers, Y. Huang, Y. Zhang, *J Mech Phys Solids* **2016**, *90*, 179.
[13] J. Liu, D. Yan, W. Pang, Y. Zhang, *Mater. Today* **2021**, *49*, 324.
[14] X. Xin, L. Liu, Y. Liu, J. Leng, *Adv. Funct. Mater.* **2020**, *30*, 2004226.
[15] S. Roh, L. B. Okello, N. Golbasi, J. P. Hankwitz, J. A. C. Liu, J. B. Tracy, O. D. Velev, *Adv. Mater. Technol.* **2019**, *4*, 1800528.
[16] Y. Su, S. Wang, Y. Huang, H. Luan, W. Dong, J. A. Fan, Q. Yang, J. A. Rogers, Y. Huang, *Small* **2015**, *11*, 367.
[17] J. A. Fan, W.-H. Yeo, Y. Su, Y. Hattori, W. Lee, S.-Y. Jung, Y. Zhang, Z. Liu, H. Cheng, L. Falgout, *Nat. Commun.* **2014**, *5*, 3266.
[18] Y. Zhang, H. Fu, S. Xu, J. A. Fan, K.-C. Hwang, J. Jiang, J. A. Rogers, Y. Huang, *J Mech Phys Solids* **2014**, *72*, 115.
[19] B. B. Mandelbrot, B. B. Mandelbrot, *The fractal geometry of nature*, WH freeman, New York **1982**.
[20] D. Avnir, O. Biham, D. Lidar, O. Malcai, *Science* **1998**, *279*, 39.
[21] M. Lewis, D. C. Rees, *Science* **1985**, *230*, 1163.

[22] L. M. Sander, *Nature* **1986**, *322*, 789.
[23] G. B. West, J. H. Brown, B. J. Enquist, *Science* **1997**, *276*, 122.
[24] R. J. Metzger, O. D. Klein, G. R. Martin, M. A. Krasnow, *Nature* **2008**, *453*, 745.
[25] C. Bovill, C. Bovill, **1996**.
[26] D. Rayneau-Kirkhope, Y. Mao, R. Farr, *Phys. Rev. Lett.* **2012**, *109*, 204301.
[27] A. Fitter, T. Stickland, *Funct. Ecol.* **1992**, 632.
[28] F. Miyamaru, Y. Saito, M. Takeda, L. Liu, B. Hou, W. Wen, P. Sheng, *Appl. Phys. Lett.* **2009**, *95*, 221111.
[29] C. Puente-Baliarda, J. Romeu, R. Pous, A. Cardama, *IEEE Trans Antennas Propag* **1998**, *46*, 517.
[30] P. Zhang, L. Chen, T. Xu, H. Liu, X. Liu, J. Meng, G. Yang, L. Jiang, S. Wang, *Adv. Mater.* **2013**, *25*, 3566.
[31] D. Wang, Q. Sun, M. J. Hokkanen, C. Zhang, F.-Y. Lin, Q. Liu, S.-P. Zhu, T. Zhou, Q. Chang, B. He, *Nature* **2020**, *582*, 55.
[32] B. C. White, A. Garland, R. Alberdi, B. L. Boyce, *Addit. Manuf.* **2021**, *38*, 101741.
[33] Q. Ge, Z. Chen, J. Cheng, B. Zhang, Y.-F. Zhang, H. Li, X. He, C. Yuan, J. Liu, S. Magdassi, *Sci. Adv.* **2021**, *7*, eaba4261.
[34] M. Lei, W. Hong, Z. Zhao, C. Hamel, M. Chen, H. Lu, H. J. Qi, *ACS Appl. Mater. Interfaces* **2019**, *11*, 22768.
[35] X. Sun, L. Yue, L. Yu, H. Shao, X. Peng, K. Zhou, F. Demoly, R. Zhao, H. J. Qi, *Adv. Funct. Mater.* **2022**, *32*, 2109805.
[36] J. W. Boley, W. M. Van Rees, C. Lissandrello, M. N. Horenstein, R. L. Truby, A. Kotikian, J. A. Lewis, L. Mahadevan, *Proc. Natl. Acad. Sci. USA* **2019**, *116*, 20856.
[37] Z. Ding, C. Yuan, X. Peng, T. Wang, H. J. Qi, M. L. Dunn, *Sci. Adv.* **2017**, *3*, e1602890.
[38] M. Safar, J. Blacher, J. Mourad, G. London, *Stroke* **2000**, *31*, 782.
[39] M. Vatankhah-Varnosfaderani, W. F. Daniel, M. H. Everhart, A. A. Pandya, H. Liang, K. Matyjaszewski, A. V. Dobrynin, S. S. Sheiko, *Nature* **2017**, *549*, 497.
[40] D. Veronda, R. Westmann, *J. Biomech.* **1970**, *3*, 111.
[41] N. N. Jason, S. J. Wang, S. Bhanushali, W. Cheng, *Nanoscale* **2016**, *8*, 16596.
[42] Y.-F. Zhang, Z. Li, H. Li, H. Li, Y. Xiong, X. Zhu, H. Lan, Q. Ge, *ACS Appl. Mater. Interfaces* **2021**, *13*, 41414.
[43] R. Lopes, N. Betrouni, *Med Image Anal* **2009**, *13*, 634.